Supporting Information

Interfacial Band Alignment and Photoelectrochemical Properties of All-Sputtered BiVO$_4$/FeNiO$_x$ and BiVO$_4$/FeMnO$_x$ *p-n* Heterojunctions

Andressa S. Correa[a†], Lucas G. Rabelo[a†], Washington S. Rosa[a], Satheesh Krishnamurthy[c], Niqab Khan[a,b], Sherdil Khan[b] and Renato V. Gonçalves[a].*

[a] São Carlos Institute of Physics, University of São Paulo, PO Box 369, 13560-970 São Carlos, SP, Brazil.

[b] Laboratory of Nanomaterials for Renewable Energy and Artificial Photosynthesis (NanoREAP), Federal University of Rio Grande do Sul (UFRGS), Campus do Vale, Agronomia, Porto Alegre-RS, Brazil.

[c] School of Engineering and Innovation, The Open University, Milton Keynes, MK7 6AA, United Kingdom

[†]Andressa S. Correa and Lucas G. Rabelo contributed equally to this paper.

1. Fabrication of the BiVO₄ ceramic target

$BiVO_4$ ceramic disks (2 inches in diameter and 3 mm thick) were synthesized through conventional solid-state reactions for use as sputtering targets. Initially, the precursor powders consisting of V_2O_5 (99.6%, Alfa Aesar) and Bi_2O_3 (99.5%, Alfa Aesar) were weighted in the correct stoichiometry and mechanically ball-milled for 24 h in a polyethylene container with zirconia cylinders and isopropyl alcohol. The resulting wet oxide mixture was dried to remove the alcohol and calcined at 500 °C for 1 h. Afterward, the as-calcined powders were mechanically ball-milled for 24 hours and then pressed at 15 MPa to produce a 55-mm-diameter disk. Finally, the as-compacted $BiVO_4$ target was sintered at 800 °C for 2 hours in an air atmosphere to achieve the desired crystalline phases and densification (> 80% of theoretical density).

Figure S1 shows the XRD patterns and Raman spectra of the as-calcined powder and $BiVO_4$ ceramic target, clearly evidencing the formation of the monoclinic-scheelite crystalline phase of $BiVO_4$, without the presence of impurities or contaminations (see discussion of the XRD pattern and Raman spectra of bare BVO film in the manuscript for a more detailed and similar analysis).
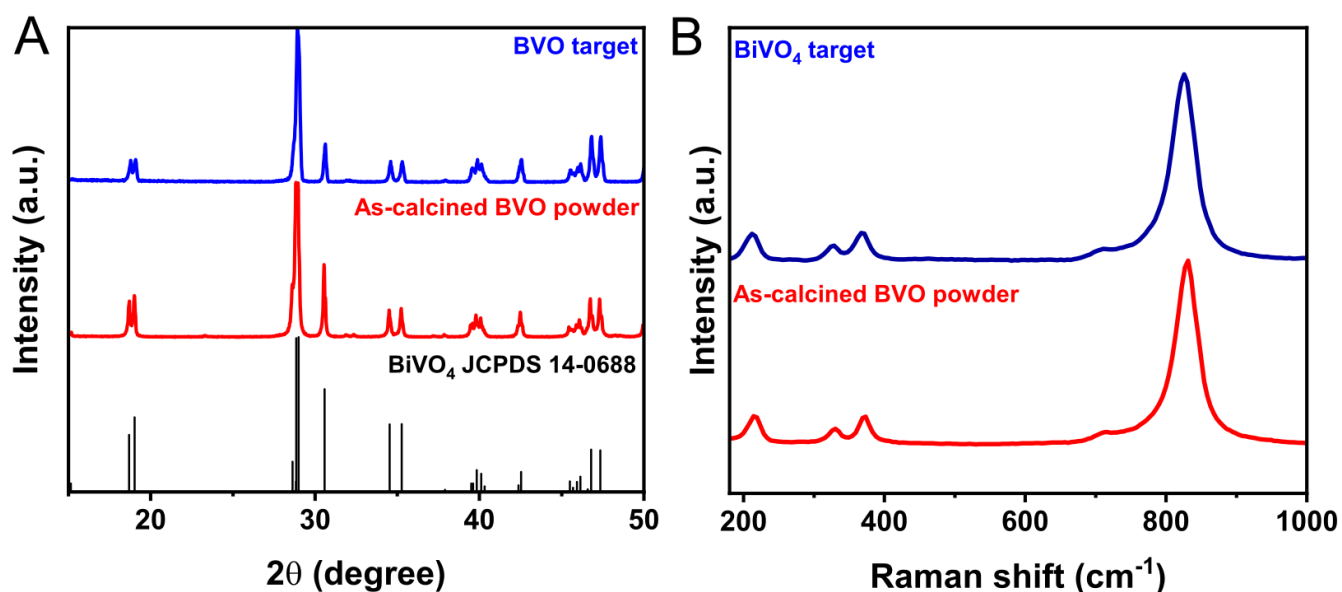
Figure S1: (a) XRD patterns and (b) Raman spectra for as-calcined $BiVO_4$ powder (prepared by solid state reaction) and $BiVO_4$ ceramic target.

2. Optimization of the deposition time of $FeMO_x$ (M = Ni, Mn) layers on the BVO film
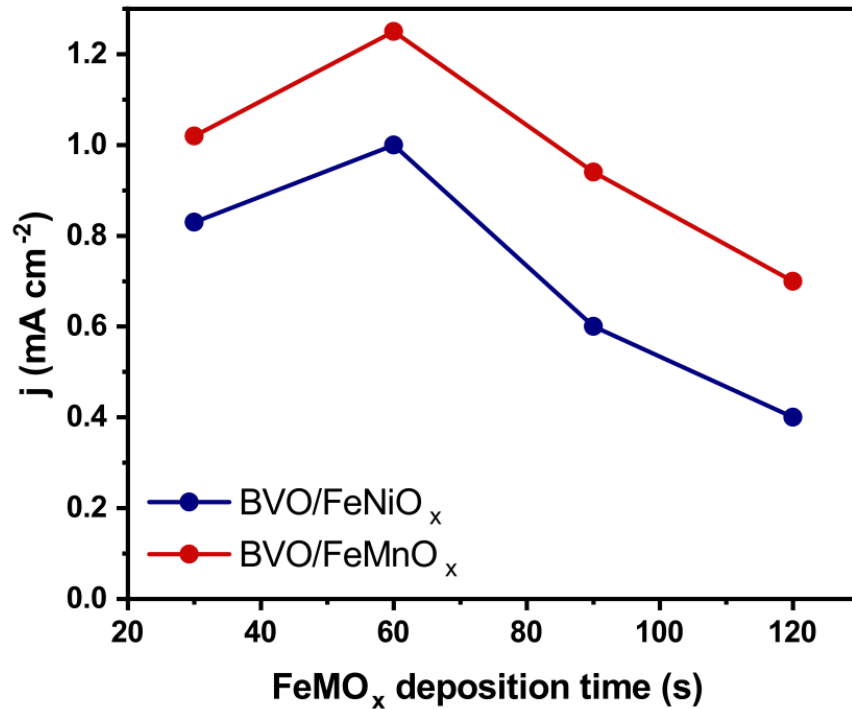

Figure S2: PEC performance of $BVO/FeMO_x$ as a function of Fe-M (M = Ni, Mn) alloy targets deposition, showing that the ideal deposition times of Fe-M alloys on the surface of bare BVO were 60 seconds for both the $FeNiO_x$ and $FeMnO_x$ compositions. The decrease of the photocurrent for longer deposition times is probably attributed to the formation of recombination centers in the $BVO/FeMO_x$ interface.

3. Deposition and characterization of bare FeMOx (M = Ni, Mn) films

Bare $FeNiO_x$ and $FeMnO_x$ ($FeMO_x$) films were deposited by one hour of magnetron sputtering on the surface of a cleaned FTO substrate using different metal alloy targets: FeMn (50 wt. % Fe and 50 wt. % Mn, 99.9% purity) and FeNi (50 wt. % Fe and 50 wt. % Ni, 99.9% purity), with an Ar/O_2 (18.5:2.1 scm) working pressure of 4.0×10^{-2} torr. All depositions were carried

out at a constant distance of 5.0 cm between the targets and FTO substrates. Prior to the initial deposition of the $BiVO_4$ target, a 30 minutes pre-sputtering deposition was performed to ensure that any potential contaminants on the surface of the target were removed.

XRD patterns for bare $FeMO_x$ (M = Ni, Mn) films deposited on FTO subtrate are shown in Fig. S3A. The absence of prominent diffraction peaks in $FeNiO_x$ and $FeMnO_x$ films confirms their predominantly amorphous nature (the observed peaks arise from the FTO substrate), which is consistent with the principles of RF-magnetron sputtering. In addition, Tauc plots of the bare $FeMO_x$ (M = Ni, Mn) films were used to estimate the optical bandgap of these compounds. According to Fig. S3B, the $FeNiO_x$ and $FeMnO_x$ exhibit direct bandgap energy of 2.32 and 2.15 eV, respectively.
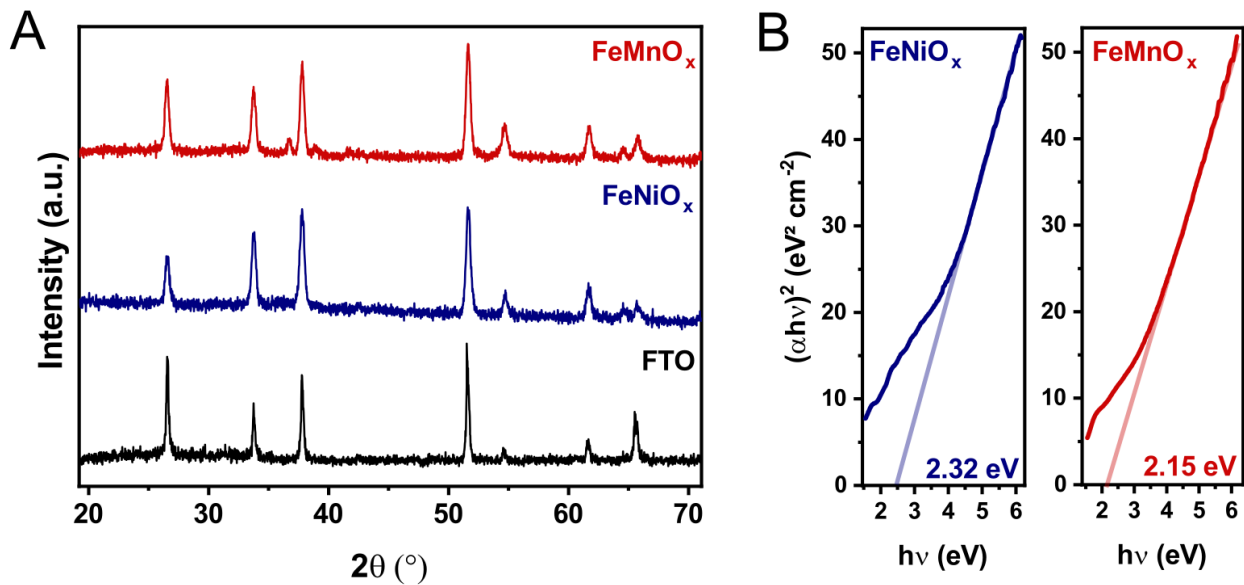

Figure S3: Characterization of bare $FeMO_x$ (M = Ni, Mn) films. (A) XRD patterns and (B) Tauc plot analysis.
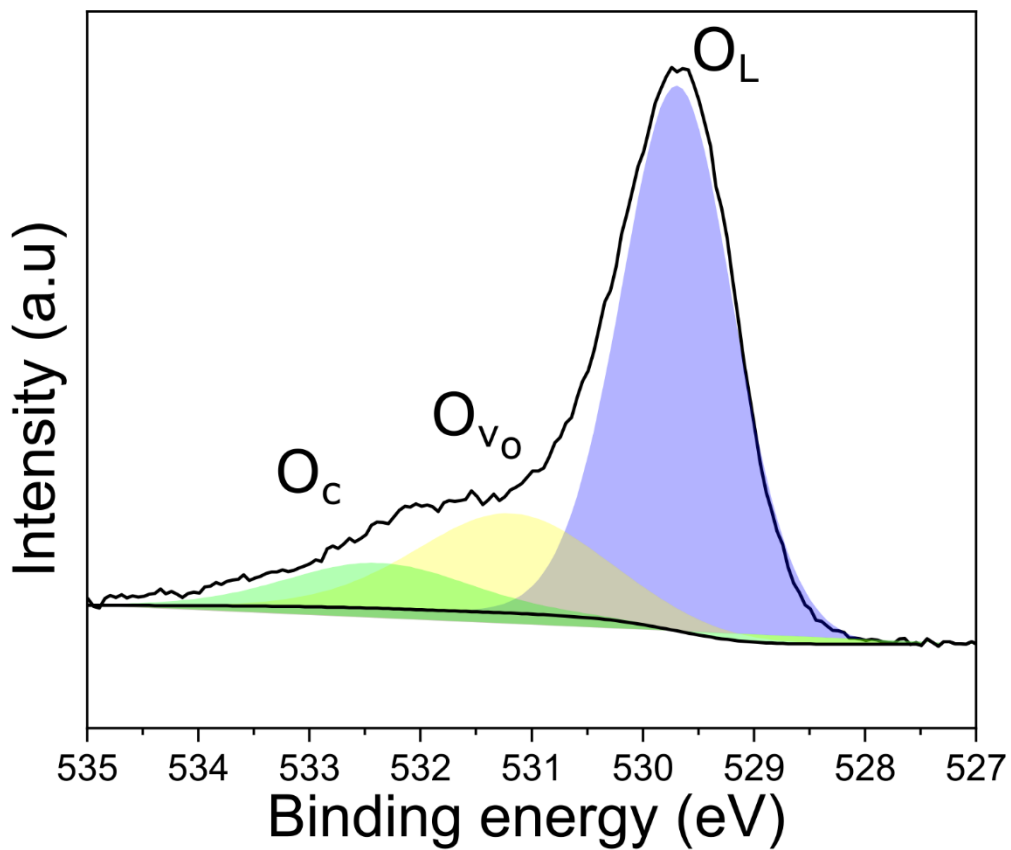
Figure S4. High-resolution O1s XPS spectra of bare $BiVO_4$ annealed at 400 °C for 1 hour.
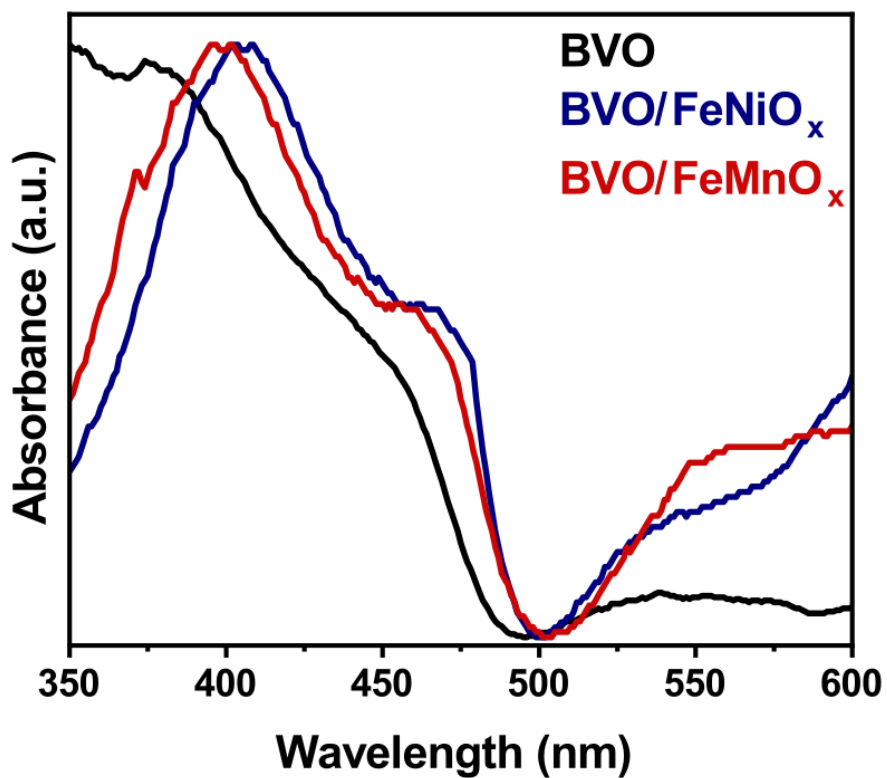
Figure S5: UV-Vis absorption spectra of bare BVO and BVO/FeMO$_x$ (M = Ni, Mn) films, evidencing the red-shift of the absorption onsets of heterostructured films compared to bare BVO. Herein, the absorbance profiles are normalized.
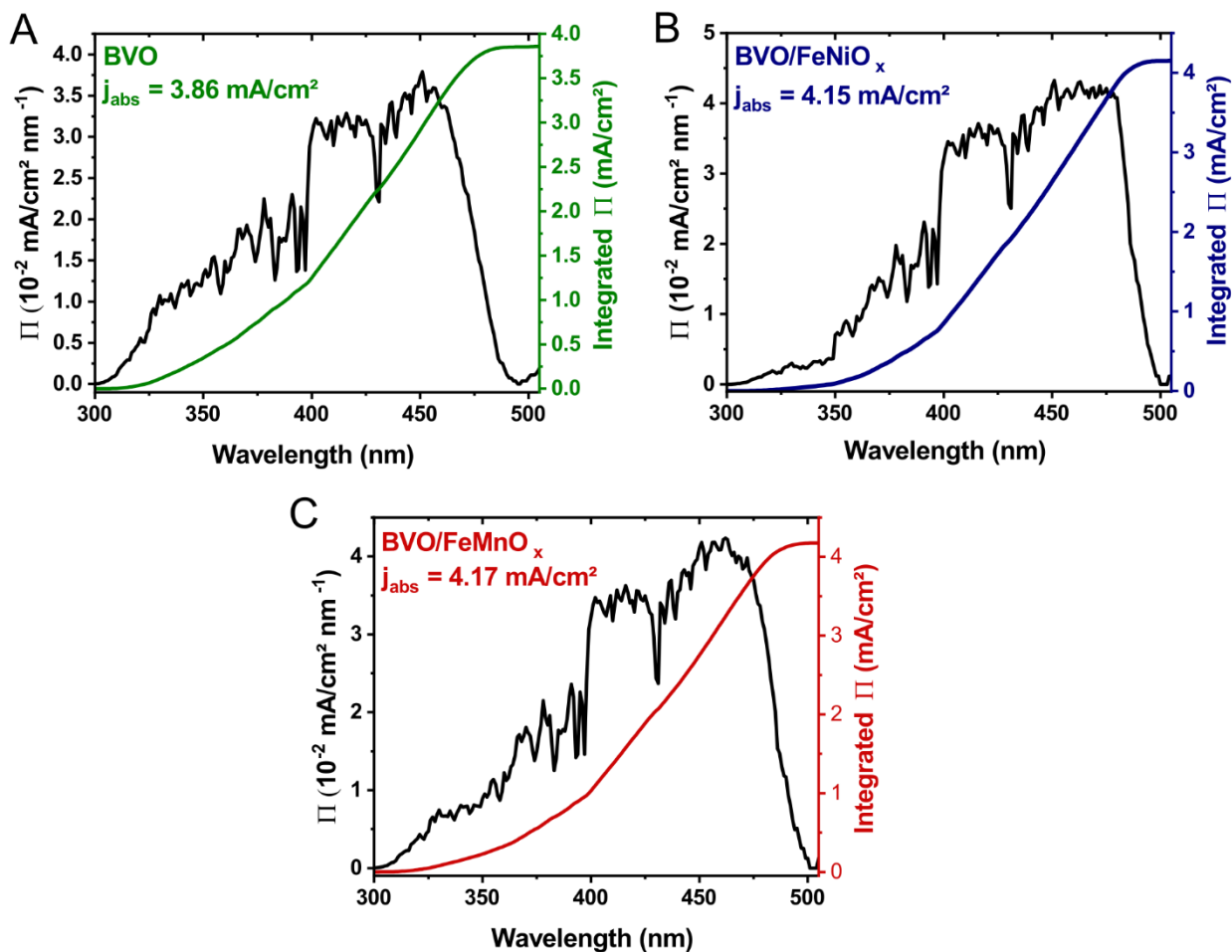

Figure S6: Absorption currents of bare BVO and BVO/FeMO$_x$ (M = Ni, Mn) films. Herein, **Π** represents the integrand of equation 4.
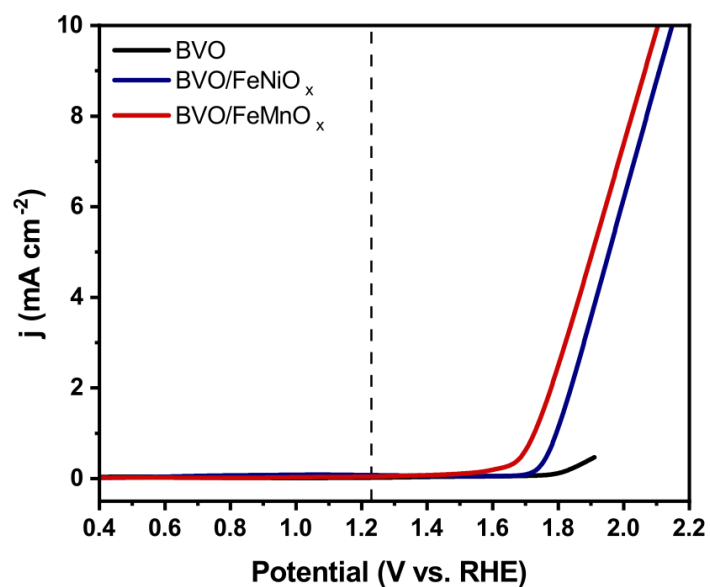
Figure S7: Current density as a function of applied potential and (B) Tafel curves for the bare FeMOx (M = Ni, Mn) films.

Importantly, several electrochemical kinetic parameters (obtained in dark conditions) provide valuable information on the role of cocatalysts in (photo)electrochemical performance.[1–3] The overpotential, in particular, is defined as the potential necessary to obtain a given (photo)current density from the water oxidation potential (+1.23 V vs. RHE), which is generally specified as 10 mA cm^{-2} (representing the approximate current density for a 10% solar-to-fuel conversion device). Therefore, photoanodes with lower overpotentials have a superior catalytic response for PEC applications.
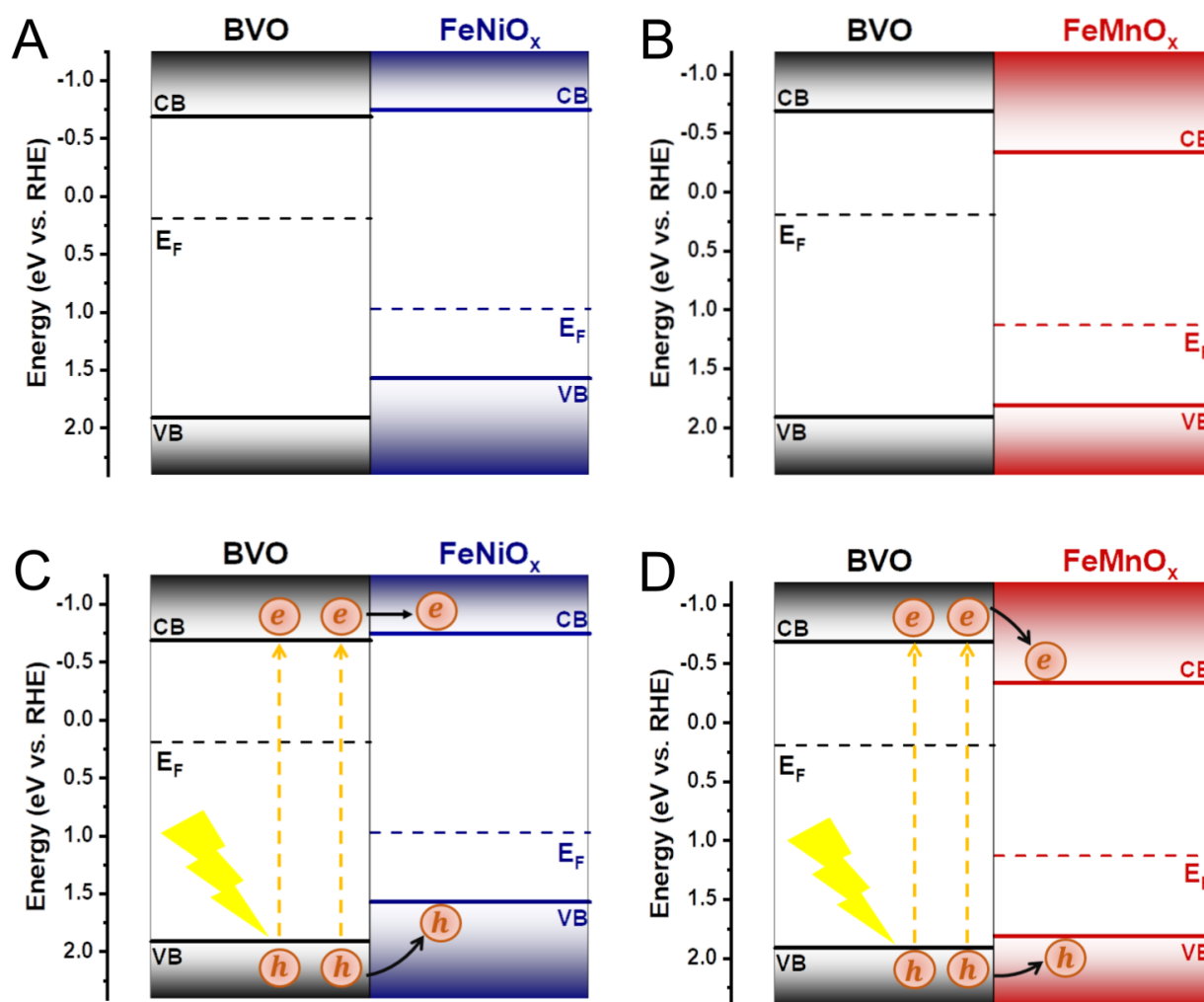
Figure S8: Traditional band alignment based on flat band diagrams of $BiVO_4$ and FeMOx (M= Ni and Mn) layers. Band diagrams at dark condition (equilibrium) for (A) $BVO/FeNiO_x$ and (B) $BVO/FeMnO_x$. Band diagrams under AM 1.5G illumination and forward applied bias: (C) $BVO/FeNiO_x$ and (D) $BVO/FeMnO_x$. Note that, despite the type II alignment, there is a high probability that the photogenerated electrons in the CB of BVO diffuse into the CB of $FeNiO_x$ (at room temperature). In contrast, the $BVO/FeMnO_x$ heterojunction exhibits a typical type I alignment with the photogenerated charge carrier pathways shown in Figure S8D.
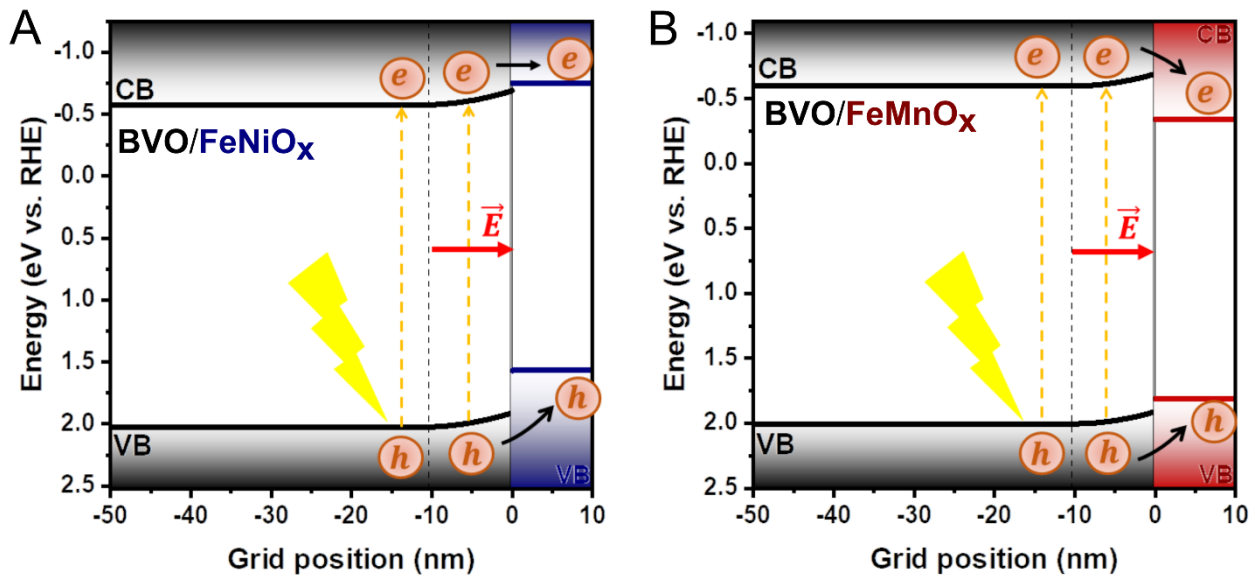
Figure S9: Qualitative classical band bending model under AM 1.5G illumination and forward external bias for (A) BVO/FeNiOₓ and (B) BVO/FeMnOₓ. Note that, despite the type II alignment, there is a high probability that the photogenerated electrons in the CB of BVO diffuse into the CB of FeNiOₓ (at room temperature). Precisely, the space charge region (SCR) is considerably reduced by the presence of photogenerated charges. In this case, the built-in electric field is significantly weakened and may not be sufficient to prevent the flow of electrons from BVO to FeNiOₓ (or FeMnOₓ) layer.

4. Band alignment model

Consider a heterojunction formed in the point $x = 0$ between an *n*-type semiconductor and a *p*-type semiconductor. As shown in Fig. S0.2a, assume semiconductors with different bandgap energies ($E_{G,n}$ and $E_{G,p}$), work functions (ϕ_n and ϕ_p) and electronic affinities (χ_n and χ_p), where work function and electronic affinity are defined, respectively, as the energy required to remove an electron from the Fermi level and the conduction band edge to a position just outside of the material (vacuum level). Figure S0.2b exhibits the band diagrams after the equilibrium of the semiconductors, evidencing the Fermi level equilibration and the development of a built-in

potential, given by the difference between the electronic affinities or Fermi energies (also defined as the sum of the potential drops induced in the *p* and *n* layers):

$$\psi_{bi} = |\phi_p - \phi_n| = \frac{(E_{F,p} - E_{F,n})}{q} = \psi_n + \psi_p \tag{S.1}$$
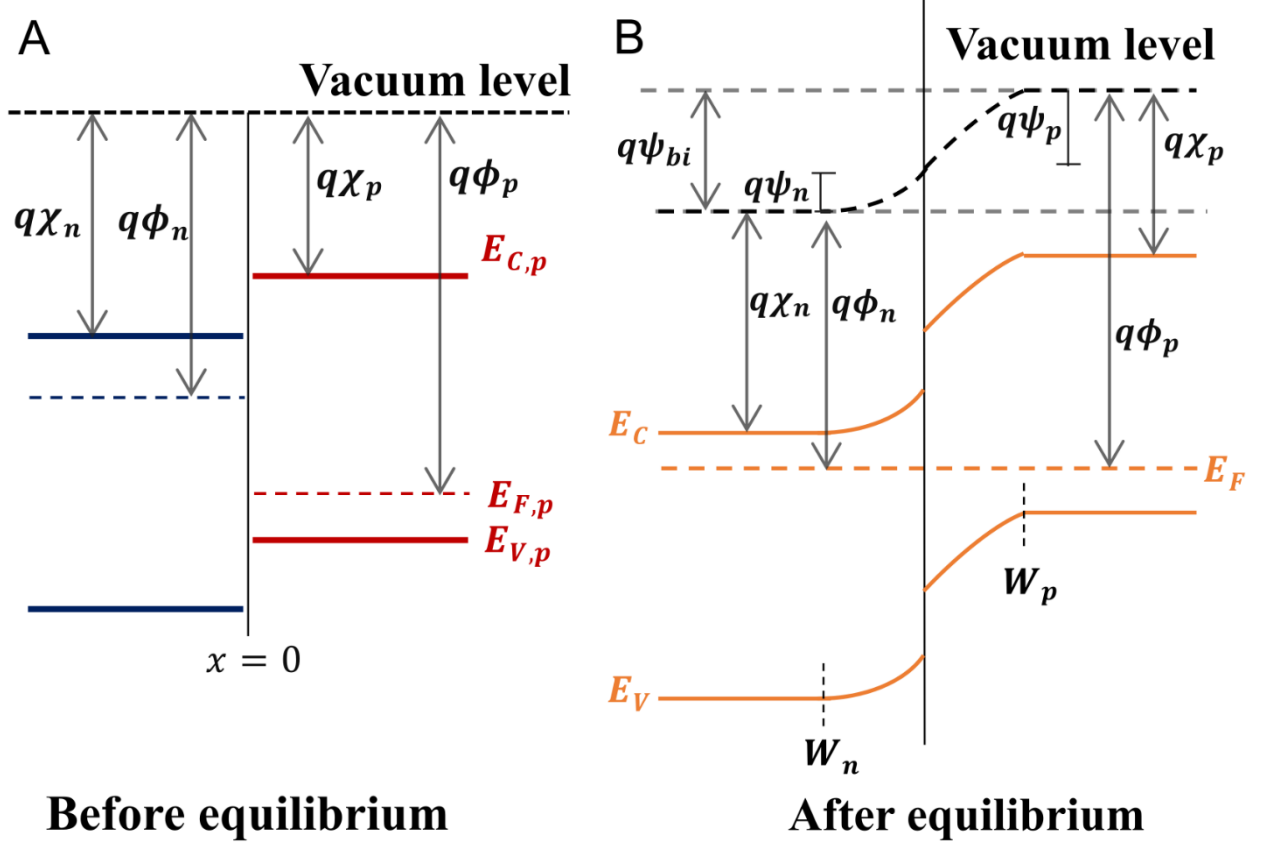

Fig. S02: Band alignment of an "abrupt" p-n heterojunction (a) before and (b) after equilibrium.

To access the interface effects on the *p-n* heterojunction, we must solve the one-dimensional Poisson equation within the space charge region, where assuming complete ionization of the dopant concentrations, it is given by:

$$\frac{d^2}{dx^2}V(x) = \begin{cases} \dfrac{qN_D}{\epsilon_0\epsilon_{r,n}}, -W_D \leq x < 0 \\ \dfrac{qN_A}{\epsilon_0\epsilon_{r,p}}, 0 \leq x < W_p \end{cases} \tag{S.2}$$

where $V(x)$ is the electrostatic potential, $-qN_D$ and qN_A are, respectively, the charge density on the n and p side, $\epsilon_{r,p(n)}$ is the dielectric constant of $p(n)$ type semiconductor, and $W_{p(n)}$ is the depletion with on $p(n)$ side. Therefore, integrating the above equation twice and using the appropriate boundary conditions, we obtain[4–6]:

$$E_C(x) = \begin{cases} E_{c1} + q\psi_n, x < -W_D \\ E_{c1} + q\psi_n - \dfrac{qN_D}{2\epsilon_0\epsilon_{r,n}}(x + W_n)^2, -W_D \leq x < 0 \\ E_{c2} - q\psi_p + \dfrac{qN_A}{2\epsilon_0\epsilon_{r,p}}(x - W_n)^2, -W_D \leq x < 0 \\ E_{c2} - q\psi_p, x > W_A \end{cases} \qquad (S.3)$$

$$E_V(x) = \begin{cases} E_C + E_{G,n}, x < 0 \\ E_C + E_{G,p}, x > 0 \end{cases} \qquad (S.4)$$

where:

$$\psi_n = \frac{N_D W_n^2}{2\epsilon_0\epsilon_{r,n}} = \frac{\epsilon_{r,p}N_A}{\epsilon_{r,p}N_A + \epsilon_{r,n}N_D}\psi_{bi} \text{ and } \psi_p = \frac{N_D W_p^2}{2\epsilon_0\epsilon_{r,n}} = \frac{\epsilon_{r,n}N_D}{\epsilon_{r,p}N_A + \epsilon_{r,n}N_D}\psi_{bi}$$

$$W_n = \left(\frac{2\epsilon_0\epsilon_{r,p}N_A\psi_{bi}}{N_D(\epsilon_{r,p}N_A + \epsilon_{r,n}N_D)}\right)^{1/2} \text{ and } W_p = \left(\frac{2\epsilon_0\epsilon_{r,n}N_A\psi_{bi}}{N_A(\epsilon_{r,p}N_A + \epsilon_{r,n}N_D)}\right)^{1/2}$$

The discontinuities of the valence and conduction bands must be invariant after equilibrium since bandgap energies and electronic affinities are considered constants in this simplified model, that is:

$$|E_C^-(0) - E_C^+(0)| = |E_{C,n} - E_{C,p}| = \Delta E_C,$$

(The plus and minus signs refer to the asymptotic value approaching $x = 0$ from the left and right, respectively). The distribution of the electric field ($\xi(x)$) can be obtained through the (minus) first derivative of the electrostatic potential. It is straightforward to show that:

$$\xi(x) = \begin{cases} \dfrac{qN_D}{\epsilon_0\epsilon_{r,n}}(x + W_n), -W_D \le x < 0 \\ \dfrac{qN_A}{\epsilon_0\epsilon_{r,p}}(x - W_p), 0 \le x < W_p \end{cases} \qquad (S.5)$$

Therefore, the built-in electric field developed on the space charge region has its maximum value at the point where the junction occurs ($x = 0$), which is given by:

$$|\xi_{max}| = \frac{qN_D W_n}{\epsilon_0\epsilon_{r,n}} = \frac{qN_A W_p}{\epsilon_0\epsilon_{r,p}}, \qquad (S.8)$$

confirming that higher values of potential drops and depletion widths result in more intense built-in electric fields. The effect of AM 1.5G illumination on the interfacial band diagram was considered as a forward external bias[7] that reduces the potential drop (ψ_{bi}) by approximately 100 mV. In this case, the above equations are still valid by substituting $\psi_{bi} \to \psi_{bi} - 100\ mV$.

Table S1: Fitted R_{ct} values of BVO/FeMO$_x$ (M = Ni, Mn) heterojunctions.

Film	$R_{ct}(\Omega)$
BVO	3600±100
BVO/FeNiO$_x$	550 ± 10
BVO/FeMnO$_x$	470 ± 10

References:

1   N.-T. Suen, S.-F. Hung, Q. Quan, N. Zhang, Y.-J. Xu and H. M. Chen, *Chem. Soc. Rev.*, 2017, **46**, 337–365.

2   W. Cai, R. Chen, H. Yang, B. Tao, H.-Y. Wang, J. Gao, W. Liu, S. Liu, S.-F. Hung and B. Liu, , DOI:10.1021/acs.nanolett.0c00840.

3   R. D. L. Smith, M. S. Prévot, R. D. Fagan, Z. Zhang, P. A. Sedach, M. K. J. Siu, S. Trudel and C. P. Berlinguette, *Science (80-.).*, 2013, **340**, 60–63.

4   R. L. Anderson, *Solid. State. Electron.*, 1962, **5**, 341–351.

5   S. M. Sze and K. K. Ng, *Phys. Semicond. Devices*, , DOI:10.1002/0470068329.

6   N. Ashcroft and N. Mermin, *Solid state physics*, 1976.

7   A. Iqbal, A. Kafizas, C. Sotelo-Vazquez, R. Wilson, M. Ling, A. Taylor, C. Blackman, K. Bevan, I. Parkin and R. Quesada-Cabrera, *Cite This ACS Appl. Mater. Interfaces*, 2021, 13.